Research in Astronomy and Astrophysics, 24:095021 (12pp), 2024 September https://doi.org/10.1088/1674-4527/ad74de

The Effect of External Magnetic Field on Electron Scale Kelvin–Helmholtz Instability

D. Tsiklauri
Joule Physics Laboratory, School of Science, Engineering and Environment, University of Salford, Manchester, M5 4WT, UK; D.Tsiklauri@salford.ac.uk
Received 2024 July 18; revised 2024 August 13; accepted 2024 August 24; published 2024 September 20

Abstract

We use particle-in-cell, fully electromagnetic, plasma kinetic simulation to study the effect of external magnetic field on electron scale Kelvin–Helmholtz instability (ESKHI). The results are applicable to collisionless plasmas when, e.g., solar wind interacts with planetary magnetospheres or a magnetic field is generated in AGN jets. We find that as in the case of magnetohydrodynamic (MHD) KHI, in the kinetic regime, the presence of an external magnetic field reduces the growth rate of the instability. In the MHD case, there is a known threshold magnetic field for KHI stabilization, while for ESKHI this is to be analytically determined. Without a kinetic analytical expression, we use several numerical simulation runs to establish an empirical dependence of ESKHI growth rate, $\Gamma(B_0)\omega_{\rm pe}$, on the strength of the applied external magnetic field. We find the best fit is hyperbolic, $\Gamma(B_0)\omega_{\rm pe} = \Gamma_0\omega_{\rm pe}/(A + B\bar{B}_0)$, where Γ_0 is the ESKHI growth rate without an external magnetic field and $\bar{B}_0 = B_0/B_{\rm MHD}$ is the ratio of external and two-fluid MHD stability threshold magnetic field, derived here. An analytical theory to back up this growth rate dependence on the external magnetic field is needed. The results suggest that in astrophysical settings where a strong magnetic field pre-exists, the generation of an additional magnetic field by the ESKHI is suppressed, which implies that nature provides a "safety valve"—natural protection not to "over-generate" magnetic field by the ESKHI mechanism. Remarkably, we find that our two-fluid MHD threshold magnetic field is the same (up to a factor $\sqrt{\gamma_0}$) as the DC saturation magnetic field, previously predicted by fully kinetic theory.

Key words: instabilities – magnetic fields – plasmas – Sun: heliosphere – ISM: magnetic fields

1. Introduction

Electron scale Kelvin–Helmholtz instability (ESKHI) is a relatively new offspring (Gruzinov 2008; Alves et al. 2012; Grismayer et al. 2013; Alves et al. 2014, 2015; Miller & Rogers 2016; Mahdavi-Gharavi et al. 2020; Yao et al. 2020) of the classical version of instability that has been known since 1868 (Helmholtz 1868; Kelvin 1871). The instability occurs due to a velocity difference (i.e., shear) at an interface. The interface can be between either (i) different parts of a single fluid or (ii) two different media, as long as there is said velocity difference. As this is a mature field of research, vast amounts of literature exist on the subject. The instability can occur in the medium that is (i) magnetized or unmagnetized, i.e., with or without an external magnetic field. (ii) Also, the description and the properties of the instability significantly differ in kinetic or fluid-like regimes. We mostly focus our consideration on the kinetic description of the instability.

In general, there are two contexts for this study: collisionless plasmas found in situations were (i) solar wind interacts with planetary magnetospheres (Delamere et al. 2011; Foullon et al. 2011; Johnson et al. 2014; Delamere et al. 2021) or (ii) when a magnetic field is generated in astrophysical scenarios, such as active galactic nuclei or gamma-ray bursts (GRBs) (Gruzinov 2008; Alves et al. 2012; Grismayer et al. 2013; Alves et al. 2014, 2015).

Accepted models of GRBs rely on the presence of a background magnetic field. It appears that magnetic field energy and kinetic energy of the accelerated particles are in equipartition. This implies that the aforesaid magnetic field needs to be somehow generated (Gruzinov 2008). Alves et al. (2012) presented the first self-consistent 3D particle-in-cell (PIC) simulations of ESKHI. The main findings of this work include establishing the saturation levels of maximum equipartition values of $E_B/E_p \approx \text{few} \times 10^{-3}$, where $E_B = \int B^2/(2\mu_0)dV$ and $E_p = \int \rho v^2/2dV$ are the volume integrated magnetic and particle kinetic energy densities, respectively. Alves et al. (2012) found what factors prescribe the level of saturation of the magnetic field generated by the ESKHI, which typically occurs on electron scales, i.e., approximately 100 electron plasma periods. Set up of Alves et al. (2012), which considers a regime of equal speed electron counter-flow layers of equal number density across the interface, is relevant to GRB shocks (Piran 2005), where density shells have similar number densities and the relativistic factor is in the range $1 \leqslant \gamma_0 \leqslant 10$. PIC numerical simulations presented by Alves et al. (2014) established the generation of a sizable,

$E_B/E_p \approx$ few $\times 10^{-3}$, and large-scale direct current (DC) magnetic field component, not predicted by a linear, fluid-like description and only appearing in the kinetic regime. Alves et al. (2014) showed that the generated magnetic field appears due to the thermal expansion of electrons of one flow into the other across the shear interface. At the same time, in Alves et al. (2014) ions stay motionless due to the large mass. This electron expansion was found to form current sheets, which generate the magnetic field. Alves et al. (2014) extended previous work by Gruzinov (2008), by considering different number densities across the shear flow interface and derived a new dispersion relation. Alves et al. (2014) also considered smooth shear flow profiles such as $v_0(x)/c = 0.2\tanh(x/L)$ and found that smoother shears produce smaller ESKHI growth rates. Alves et al. (2014) in this way provided a generalization of the magnetohydrodynamic (MHD) result by Miura & Pritchett (1982), who in turn found that, in the compressible case, the growth rate is a function of the magnetic Mach number and the modes with $kL < 2$ are unstable. Miura & Pritchett (1982) also found that the most unstable modes have their wavelength comparable to the width of the shear layer $2kL \simeq 1$. A very important distinction between kinetic and MHD regimes is underscored by Alves et al. (2014), on page 9, which we quote without an alteration: "shear flow instabilities in initially unmagnetized conditions with fast drift velocities (relative to the temperature) can only develop on the electron-scale." This underscores the importance of kinetic effects which is one of the main motivations for this study in the Kelvin–Helmholtz instability (KHI) context. Alves et al. (2015) studied a new type of kinetic instability, so-called mushroom instability (MI), named so because of the mushroom-shaped features found in the electron number density. The difference between ESKHI and MI is that, for ESKHI $\boldsymbol{v}_0(x) \| Oy$, while for ESKHI, $\boldsymbol{v}_0(x) \| Oz$. Alves et al. (2015) studied how the growth rates of ESKHI and MI scale with $\beta_0 = v_0/c$ and γ_0, and found that ESKHI has higher growth rates than MI for sub-relativistic settings. However, the MI growth rate decays with $\gamma_0^{-1/2}$, slower than that of ESKHI, which decays with $\gamma_0^{-3/2}$ (see Figure 1 from Alves et al. 2015). Thus they concluded that ESKHI dominates for $\gamma_0 \approx 1$ for sub-relativistic flows, while MI dominates for $\gamma_0 \gg 1$. Because of this reason, i.e., we would like our results to be applicable to both (i) collisionless plasmas when the solar wind interacts with planetary magnetospheres or (ii) magnetic field is generated in places, such as active galactic nuclei and GRBs with relatively moderate γ_0 values, this paper focuses mostly on ESKHI with $\beta_0 = v_0/c = 0.2$ ($\gamma_0 = 1.02$)—this is the value also considered by Alves et al. (2014).

We mention in passing that, while the above discussion was for the electron-proton plasmas, a body of work exists on electron-scale kinetic, relativistic shear instabilities, where similarly, the magnetic field generation is seen but in electron-positron plasmas (Liang et al. 2013a). A comparison of the electron-positron results to electron-proton plasmas (Liang et al. 2013b; Nishikawa et al. 2014) or dependence of the growth rate on the ion-to-electron mass ratio has been also studied (Nishikawa et al. 2013).

Miller & Rogers (2016) extended the analysis of Gruzinov (2008), Alves et al. (2012, 2014, 2015) by considering warm plasmas and found that the growth rate is significantly, up to a factor of 3, larger for the case of large temperatures. This analytical calculation conclusion by Miller & Rogers (2016) is supported by the multi-dimensional PIC simulations of Grismayer et al. (2013). Yao et al. (2020) also analyzed the role of electron thermal motion effects on the generation of the magnetic field. Yao et al. (2020) found an increase in the growth rate with the increasing plasma temperature. Mahdavi-Gharavi et al. (2020) studied the instability growth rate of the excited electromagnetic modes for the relativistic and non-relativistic cases of solar wind, interacting with the interstellar plasma medium with an emphasis on the effect of the viscosity of plasma.

The above introductory comments were all in the kinetic regime. In the fluid-like description of KHI, the first paper that considered the effect of the external magnetic field on KHI was Michael (1955). It should be noted, it was Michael (1955) who first derived the dispersion relation for the simple case of an incompressible plasma with a discontinuous flow shear with the perturbations to the interface between two conducting media, with velocities U_0 and U_1 and constant magnetic fields B_0 and B_1 that are parallel to the interface. Many published works wrongly attribute this result to Chandrasekhar (1961), which is a later work. Blandford & Pringle (1976) studied linearized KHI with a calculation that generalized previous treatments to include relativistic relative motion and relativistic internal sound speeds. The study was performed in the context of beam models of extragalactic radio sources.

The motivation for the present work is two-fold: (i) To extend the MHD analysis of Michael (1955) to the kinetic regime of ESKHI; and (ii) To extend the kinetic analysis of Alves et al. (2014) by adding the effect of an external magnetic field to ESKHI.

The paper is organized as follows: Section 1 provides an introduction to the subject of ESKHI. Section 2 discusses prior analytical and numerical findings about ESKHI. Section 3 provides the details of our model. Section 4 reveals the main results of this study. Section 5 lists the main conclusions of this work.

2. Prior Analytical and Numerical Findings about ESKHI

An analytic calculation by Gruzinov (2008) provides the growth rate of ESKHI in 2D. A limited, relevant number of components of background relativistic shear flows and number

densities

$$\boldsymbol{v}_0 = (0,\, v_0(x),\, 0), \quad n_0 = n_0(x), \tag{1}$$

as well as electromagnetic field perturbations

$$\boldsymbol{E}_1 = (E_{1x}(x),\, E_{1y}(x),\, 0), \quad \boldsymbol{B}_1 = (0,\, 0,\, B_{1z}(x)), \tag{2}$$

with the perturbation wavevectors having only y-component and harmonic time dependence as $f_1 = \tilde{f}_1(x)e^{i(k_y y-\omega t)}$ were considered. Gruzinov (2008) established that for equal speed electron counter-flow layers of the same number density across the interface, i.e., for $v_0(x) = v_0\mathrm{sign}(x)$ and $n_0(x) = \mathrm{const}$, the growth rate is

$$\Gamma_0^2 = \frac{\omega_{\mathrm{pe}}^2}{2}\left(\sqrt{1 + 8\frac{k^2 v_0^2}{\omega_{\mathrm{pe}}^2}} - 1 - 2\frac{k^2 v_0^2}{\omega_{\mathrm{pe}}^2}\right). \tag{3}$$

Equation (3) then implies that the condition for the ESKHI is $|kv_0| < \omega_{\mathrm{pe}}$. Figure 3 from Alves et al. (2014) gives a graphical representation of the growth rate of ESKHI versus wavenumber. It appears like an upside down parabola, with skewed to the right maximal growth rate of

$$\Gamma_0 = \frac{\omega_{\mathrm{pe}}}{2\sqrt{2}} \approx 0.35\omega_{\mathrm{pe}}, \tag{4}$$

at the most unstable wavenumber

$$kv_0 = \frac{\sqrt{3}\,\omega_{\mathrm{pe}}}{2\sqrt{2}} \approx 0.61\omega_{\mathrm{pe}}. \tag{5}$$

Note that in the above equations, k and ω_{pe} include the relativistic factor $\gamma_0 = 1/\sqrt{1 - v_0^2/c^2}$ dependence. However, Grismayer et al. (2013) give a useful, explicit dependence on the relativistic factor γ_0, and draw a distinction between $k_\perp$ and $k_\parallel$ of the form $f_1 = \tilde{f}_1(x)e^{-k_\perp|x|}e^{i(k_\parallel y-\omega t)}$:

$$\Gamma_0^2 = \frac{\omega_{\mathrm{pe}}^2}{2\gamma_0^3}\left(\sqrt{1 + 8\frac{k_\parallel^2 v_0^2\gamma_0^3}{\omega_{\mathrm{pe}}^2}} - 1 - 2\frac{k_\parallel^2 v_0^2\gamma_0^3}{\omega_{\mathrm{pe}}^2}\right), \tag{6}$$

$$\Gamma_{0,\max} = \frac{1}{2\sqrt{2}}\gamma_0^{-3/2}\omega_{\mathrm{pe}} \approx 0.35\gamma_0^{-3/2}\omega_{\mathrm{pe}}, \tag{7}$$

$$k_{\parallel,\max}v_0 = \frac{\sqrt{3}\,\gamma_0^{-3/2}\omega_{\mathrm{pe}}}{2\sqrt{2}} \approx 0.61\gamma_0^{-3/2}\omega_{\mathrm{pe}}, \tag{8}$$

with $\omega_{\mathrm{pe}} = \sqrt{n_e e^2/(m_e\varepsilon_0)}$ being electron plasma frequency for $\gamma_0 = 1.0$, strictly.

Alves et al. (2012) performed self-consistent 3D PIC simulations to study ESKHI. They found that the saturation levels of maximum equipartition values are $E_B/E_p \approx 2\times10^{-3}$ for the sub-relativistic scenario, and $E_B/E_p \approx 7\times10^{-3}$ for the relativistic scenario. In their terminology, sub-relativistic means $\gamma_0 = 1.02$ (i.e., $v_0/c = \sqrt{1 - 1/\gamma_0^2} = 0.1971 \approx 0.2$) and relativistic means $\gamma_0 = 3$ (i.e., $v_0/c = \sqrt{1 - 1/\gamma_0^2} = 0.9428 \approx 0.9$). Also, Alves et al. (2012) and Grismayer et al. (2013) established what prescribes the level of saturation of the magnetic field generated by the ESKHI, which typically occurs on "electron scales" approximately $\approx 100/\omega_{\mathrm{pe}}$ with the saturation magnetic field given by

$$B_{\mathrm{DC}} \simeq \frac{m_e\omega_{\mathrm{pe}}}{e}\beta_0\sqrt{\gamma_0}. \tag{9}$$

Note that in Equation (9), B_{DC} is in SI units while Grismayer et al. (2013) uses CGS, hence the conversion of magnetic field and charge yields a factor of $\sqrt{\mu_0/4\pi} \times \sqrt{4\pi\varepsilon_0} = 1/c$.

3. Description of the Model

3.1. Theoretical Considerations

Because our motivation for the present work is, on one hand, to extend the MHD analysis of Michael (1955) to the kinetic regime of ESKHI and, on the other hand, to extend the kinetic analysis of Alves et al. (2014) by adding the effect of an external magnetic field to ESKHI, we need to somehow fix the relevant magnetic field scale. It is common knowledge that usually in many space and astrophysical plasma situations "MHD works where it should not," so in the absence of an analytical theory of ESKHI with an external magnetic field, we fix the relevant magnetic field scale as a two-fluid MHD stability threshold magnetic field, based on the calculation given in Appendix. In particular, Michael (1955)'s dispersion relation, for an incompressible plasma with a discontinuous flow shear and perturbations to the interface between two conducting media, with velocities U_1 and U_2 and constant magnetic fields B_1 and B_2 that are parallel to the interface, reads as

$$\frac{\omega}{k} = -\frac{U_1 + U_2}{2} \pm \sqrt{\frac{(B_1^2 + B_2^2)}{2\mu_0\rho} - \frac{\Delta U^2}{4}}, \tag{10}$$

where $\Delta U = U_1 - U_2$ is the flow velocity difference across the interface. Equation (10) thus suggests the existence of stability threshold magnetic fields that satisfy

$$\frac{(B_1^2 + B_2^2)}{2\mu_0\rho} = \frac{\Delta U^2}{4}. \tag{11}$$

Special cases are: (i) a case without external magnetic field $B_1 = B_2 = 0$ that recovers the KH result that the current sheet is always unstable as long as there is a velocity difference; and (ii) a case of $U_1 = -U_2 = v_0$ and $B_1 = B_2 = B_0$ considered in this paper, then the stability threshold magnetic field is

$$\frac{B_0^2}{2\mu_0} = \rho\frac{v_0^2}{2}, \tag{12}$$

which physically means that the threshold magnetic field is achieved when the magnetic field energy density is equal to counter-flow kinetic energy density.

In the kinetic description, the electron dynamics is crucial, while massive ions essentially provide a neutralizing background.

For example, the Alves et al. (2014) calculation pertains to moving electrons only. We therefore make an important change to Equation (12), namely, $\rho \rightarrow \rho_e = n_e m_e$. This means switching to a two-fluid MHD with $\boldsymbol{v} \rightarrow \boldsymbol{v}_e$, i.e., opposite to a single fluid MHD in which electrons and ions are "glued" to each other and act as a single fluid. Thus, for the purposes of this paper, based on Equation (12), we set

$$B_{\rm MHD} = \sqrt{\mu_0 m_e n_e}\, v_0. \tag{13}$$

Using the definition of electron plasma frequency $\omega_{\rm pe} = \sqrt{n_e e^2/(m_e \varepsilon_0)}$ and the expression $c = 1/\sqrt{\mu_0 \varepsilon_0}$, Equation (13) can be rewritten in the notations of Equation (9) as

$$B_{\rm MHD} = \frac{m_e \omega_{\rm pe}}{e}\left(\frac{v_0}{c}\right) = \frac{m_e \omega_{\rm pe}}{e}\beta_0. \tag{14}$$

It is remarkable that Grismayer et al. (2013)'s Equation (9) and our (14) are the same, up to a factor of $\sqrt{\gamma_0}$. In other words, a two-fluid MHD threshold magnetic field, derived here—see Appendix for the derivation of the extended version of Equation (10)—which suppresses the KH instability, is the same (up to a factor of $\sqrt{\gamma_0}$ which is 1.02 for the present paper) as the DC saturation magnetic field predicted by the kinetic theory and simulations of Grismayer et al. (2013).

We specifically refrain from using the terms electron MHD or electromagnetohydrodynamic (EMHD) which have a more specific meaning. Instead, we refer to "two-fluid MHD," as it would be more precise, but too cumbersome to use the term "two-fluid MHD with stationary ions." The following discussion explains why: According to Lyutikov (2013), who in turn, based his discussion on Gordeev et al. (1994), within the framework of EMHD, the entire electric current is carried by an electron fluid: $\boldsymbol{J} = -en_e\boldsymbol{v}_e$, ions only provide a neutralizing background and do not move, i.e., do not contribute to pressure or mass (inertia). For the case of infinite conductivity, the magnetic field is frozen into electron fluid and thus an electric field satisfies the condition

$$\boldsymbol{E} + \boldsymbol{v}_e \times \boldsymbol{B} = 0. \tag{15}$$

Hence, the magnetic field induction equation is of the form

$$\frac{\partial \boldsymbol{B}}{\partial t} = \nabla \times (\boldsymbol{v}_e \times \boldsymbol{B}). \tag{16}$$

In the EMHD approximation, the next crucial step is replacing $\boldsymbol{v}_e$ in Equation (16) using the current expression $\boldsymbol{v}_e = -\boldsymbol{J}/(en_e)$, where $\boldsymbol{J} = \nabla \times \boldsymbol{B}/\mu_0$, i.e., $\boldsymbol{v}_e = -\nabla \times \boldsymbol{B}/(\mu_0 e n_e)$

$$\frac{\partial \boldsymbol{B}}{\partial t} = -\frac{1}{\mu_0 e}\nabla \times \left[\frac{(\nabla \times \boldsymbol{B})}{n_e} \times \boldsymbol{B}\right]. \tag{17}$$

Cho & Lazarian (2009) provide a rigorous physical interpretation for the EMHD approximation, by considering MHD, Hall MHD, and EMHD at appropriate spatial scales. They use ion inertial length, $d_i = c/\omega_{\rm pi}$, for their ordering of terms (see discussion around their Equations (8)–(13)). We instead use electron inertial length, $d_e = c/\omega_{\rm pe}$. In the Hall MHD approximation, one has

$$\frac{\partial \boldsymbol{B}}{\partial t} = \nabla \times (\boldsymbol{v} \times \boldsymbol{B}) - \frac{1}{\mu_0 e}\nabla \times \left[\frac{(\nabla \times \boldsymbol{B})}{n_e} \times \boldsymbol{B}\right]. \tag{18}$$

Note that in Equation (18) the first term contains the bulk plasma velocity $\boldsymbol{v}$, not the electron one $\boldsymbol{v}_e$. In Equations (17) and (18) the factor $1/(\mu_0 e n_e)$ can be written as $1/(\mu_0 e n_e) = d_e^2 e/m_e$. Now expressing e/m_e using Equation (14) we get $1/(\mu_0 e n_e) = d_e^2 \omega_{\rm pe} v_0/(B_0 c)$. Hence with the substitution in Equation (18) of $\boldsymbol{v} \simeq v_0$, $\nabla \simeq 1/L_0$, and $\nabla t \simeq 1/T_0$, the different term ordering is

$$\frac{B_0}{T_0} \simeq \frac{B_0 v_0}{L_0} - \left(\frac{d_e}{L_0}\right)\frac{B_0 v_0}{L_0}. \tag{19}$$

Thus, from Equation (19) it follows that for spatial scales much larger than electron inertial length $L_0 \gg d_e$, usual single fluid MHD applies while on scales $d_e \ll L_0$ EMHD applies. But ESKHI is not at that scale, rather it is at a scale of $L_0 \simeq d_e$. That is why we refrain from the use of the term EMHD.

We also mention a useful notation of the magnetic field induction in the EMHD approximation provided by Zhao et al. (2010)

$$\frac{\partial (1 - d_e^2\nabla^2)\boldsymbol{B}}{\partial t} = \nabla \times (\boldsymbol{v}_e \times (1 - d_e^2\nabla^2)\boldsymbol{B}). \tag{20}$$

Note that Equation (20) reduces to Equation (16) with $d_e^2\nabla^2 = d_e^2/L_0^2 \ll 1$.

With this distinction clearly stated, we refrain from using the induction equation in the form of Equation (17), and we stick with Equation (16) rewritten as in Michael (1955). In the Appendix, we provide a calculation similar to Michael (1955), but with different densities on either side of the shear interface and with the substitution $\boldsymbol{v} \rightarrow \boldsymbol{v}_e$ and $\rho \rightarrow \rho_e$, since only electrons move and stationary ions cannot contribute to the mass (inertia). We now state the main, starting equations of two-fluid MHD with stationary ions:

$$\frac{\partial \boldsymbol{B}}{\partial t} + (\boldsymbol{v}_e \cdot \nabla)\boldsymbol{B} = (\boldsymbol{B} \cdot \nabla)\boldsymbol{v}_e, \tag{21}$$

$$\frac{\partial \boldsymbol{v}_e}{\partial t} + (\boldsymbol{v}_e \cdot \nabla)\boldsymbol{v}_e = -\frac{\nabla p_e}{\rho_e} + \frac{(\nabla \times \boldsymbol{B}) \times \boldsymbol{B}}{\mu_0 \rho_e}, \tag{22}$$

$$\nabla \cdot \boldsymbol{v}_e = 0, \quad \nabla \cdot \boldsymbol{B} = 0. \tag{23}$$

In the Appendix we derive the two-fluid MHD dispersion relation for the different electron densities, ρ_{e1} and ρ_{e2}, on either side of the interface, where we obtain:

$$\frac{\omega}{k} = -\frac{U_{e1}\rho_{e1} + U_{e2}\rho_{e2}}{(\rho_{e1} + \rho_{e2})} \pm \sqrt{\frac{(B_1^2 + B_2^2)}{\mu_0(\rho_{e1} + \rho_{e2})} - \frac{\rho_{e1}\rho_{e2}\Delta U_e^2}{(\rho_{e1} + \rho_{e2})^2}}, \tag{24}$$

where $\Delta U_e = U_{e1} - U_{e2}$.

For the same electron density ρ_e on either side of the interface, we obtain

$$\frac{\omega}{k} = -\frac{U_{e1}+U_{e2}}{2} \pm \sqrt{\frac{(B_1^2+B_2^2)}{2\mu_0\rho_e} - \frac{\Delta U_e^2}{4}}, \quad (25)$$

and further still with $U_{e1} = -U_{e2} = v_0$, i.e., $\Delta U_e = 2v_0$ and $B_1 = B_2 = B_0$ considered in this paper, we obtain

$$\frac{\omega}{k} = 0 \pm \sqrt{\frac{B_0^2}{\mu_0\rho_e} - \frac{\Delta U_e^2}{4}}. \quad (26)$$

Defining the *electron*-scale Alfvén speed as $V_{Ae} = B_0/\sqrt{\mu_0\rho_e}$, then according to Equation (26) the stability threshold is

$$\Delta U_e > 2V_{Ae} \quad \text{or} \quad v_0 > V_{Ae}. \quad (27)$$

We also note that for the above conditions, the real part of frequency is zero, $\omega_r = 0$.

A word of caution is that we are fully aware of the fact that Equations (21)–(23) ignore the displacement current which means that relativistic effects are ignored because in fluid theory ratio of electric field and magnetic forces is of the order $(|\rho_e \boldsymbol{E}|/|\boldsymbol{j} \times \boldsymbol{B}|) \simeq v_0^2/c^2$. The numerical runs presented in this paper are for $v_0^2/c^2 = 0.2^2 = 0.04 \ll 1$ so the above equations are valid. We are also aware that a proper calculation should follow a similar approach as Alves et al. (2014, 2015) where the electric field (the displacement current) effect is explicitly present. Hence, we remark that an analytical theory to back up the growth rate dependence on the external magnetic field is outstanding and still needed. We stress that we only use the calculations based on Equations (21)–(23), and their outcomes just set the scale of the two-fluid (non-relativistic) MHD stability threshold magnetic field, given by Equations (13) and (14).

3.2. Numerical Simulation Considerations

In this work, we use the 2.5D version of the PIC code EPOCH. This is a 1.5, 2.5, and 3D, fully electromagnetic, PIC code (Arber et al. 2015). In order to be able to use periodic boundary conditions throughout, which we remark, are the most precise boundary conditions for the numerical implementation, we implement a "sandwich" with three layers of plasma with the following properties: two down-flow layers satisfying $x/L_x < 0.25$ or $x/L_x > 0.75$ with velocity $v_0/c = -0.2$ and one up-flow layer with $0.25 < x/L_x < 0.75$ with velocity $v_0/c = 0.2$ in between and v_0 being parallel to Oy axis. The system size is $(L_x, L_y) = (10c/\omega_{pe}, 5c/\omega_{pe})$ which is resolved with a 200×100 grid. This means each grid cell has a size of $1/20$ of c/ω_{pe}, i.e., $\Delta_x = \Delta_y = 0.05c/\omega_{pe}$. The maximal temperature is set as $T_{e,i,\,max} = m_e(0.005c)^2/k_B = 148239.77$ K. This ensures a cold plasma approximation because $v_{th,e} = \sqrt{k_B T_{e,i,max}/m_e} = 0.005c \ll v_0 = 0.2c$. The reason we refer to the maximal temperature is because it actually varies across the x-axis. This is because as in Tsiklauri (2023) we keep pressure balance by making $p_{e,i} = n_{e,i}(x)kT_{e,i}(x) = \text{const}$, i.e., $T_{e,i}(x) = T_{e,i,max}[n_0/n_{e,i}(x)] \propto 1/n_{e,i}(x)$. With the magnetic field being uniform $B_{y0} = \bar{B}_0 B_{MHD} = \bar{B}_0\sqrt{\mu_0 m_e n_e} v_0$, given by Equation (13), this means that total initial pressure balance $p_{e,i} + B^2/(2\mu_0) = \text{const}$ is satisfied. The factor $\bar{B}_0 = 0, 0.5, 1.0, 5.0, 7.5, 10.0, 15.0$ provides a variation of the external magnetic field, with $B_{y0}/B_{MHD} = 0, <1, 1, \gg 1$. The electron and ion number densities are set as follows: For the down-flows

$$n_{e,i}(x) = \begin{cases} n_0, & \text{if } (x < 0.25L_x) \text{ or } (x > 0.75L_x) \\ 10^{-2}n_0, & \text{otherwise} \end{cases}. \quad (28)$$

For the up-flow, vice versa

$$n_{e,i}(x) = \begin{cases} 10^{-2}n_0, & \text{if } (x < 0.25L_x) \text{ or } (x > 0.75L_x) \\ n_0, & \text{otherwise} \end{cases}. \quad (29)$$

The factor 10^{-2}, while dropping density to nearly zero, stops EPOCH from slowing down for numerical reasons. In EPOCH code physical quantities are in SI units, so we fix $n_0 = 10^{15}$ particles per m^{-3}, typical of many collisionless astrophysical plasmas. The terms up-flow and down-flow only refer to motions figurally up and down the Oy axis, as there is no gravity present in our simulations or calculations. The plasma consists of electrons and protons with the realistic mass ratio $m_p/m_e = 1836$. Both electrons and ions are mobile throughout the simulation. At $t = 0$ electron and ion velocities are set as described above, i.e., a "sandwich" with three layers of plasma. This ensures that initially there is zero net current. We force the initial zero-net-current condition because when ions are stationary (these results are not included here), strong oscillations with electron plasma frequency ω_{pe} appear, e.g., in $(E_B - E_B(0))/E_p(0)$ and $(E_p - E_p(0))/E_p(0)$, in Figures 3 and 5, respectively. Thus, the zero-net-current condition is necessary to study a clear effect of the external magnetic field on ESKHI, not marred by the said oscillations. In the EPOCH implementation we effectively load four plasma species, electron and proton up-flows, and down-flows as specified by Equations (28) and (29). We use 200 particles per cell for each species. so in total, we have $4 \times 200 \times 200 \times 100 = 1.6 \times 10^7$ particles. One numerical run takes approximately 40 minutes on 12 processor cores. In this paper, we only show snapshots of electron number density n_e and the magnetic field B_z component generated by ESKHI normalized on $B_{MHD} = (m_e\omega_{pe}/e)(v_0/c)$. The length is normalized by c/ω_{pe}. The end simulation time is set to $150/\omega_{pe}$.

4. The Results

In Figure 1 we display snapshots of electron number density n_e, which is the sum of down and up-flowing electrons. The row of panels (a), (b), and (c) shows n_e/n_0 for Run 0 at times $t = 20$, 25, $30/\omega_{pe}$ respectively. The row of panels (d), (e), and (f) shows n_e/n_0 for Run 2 at times $t = 20$, 25, $30/\omega_{pe}$ respectively. The row

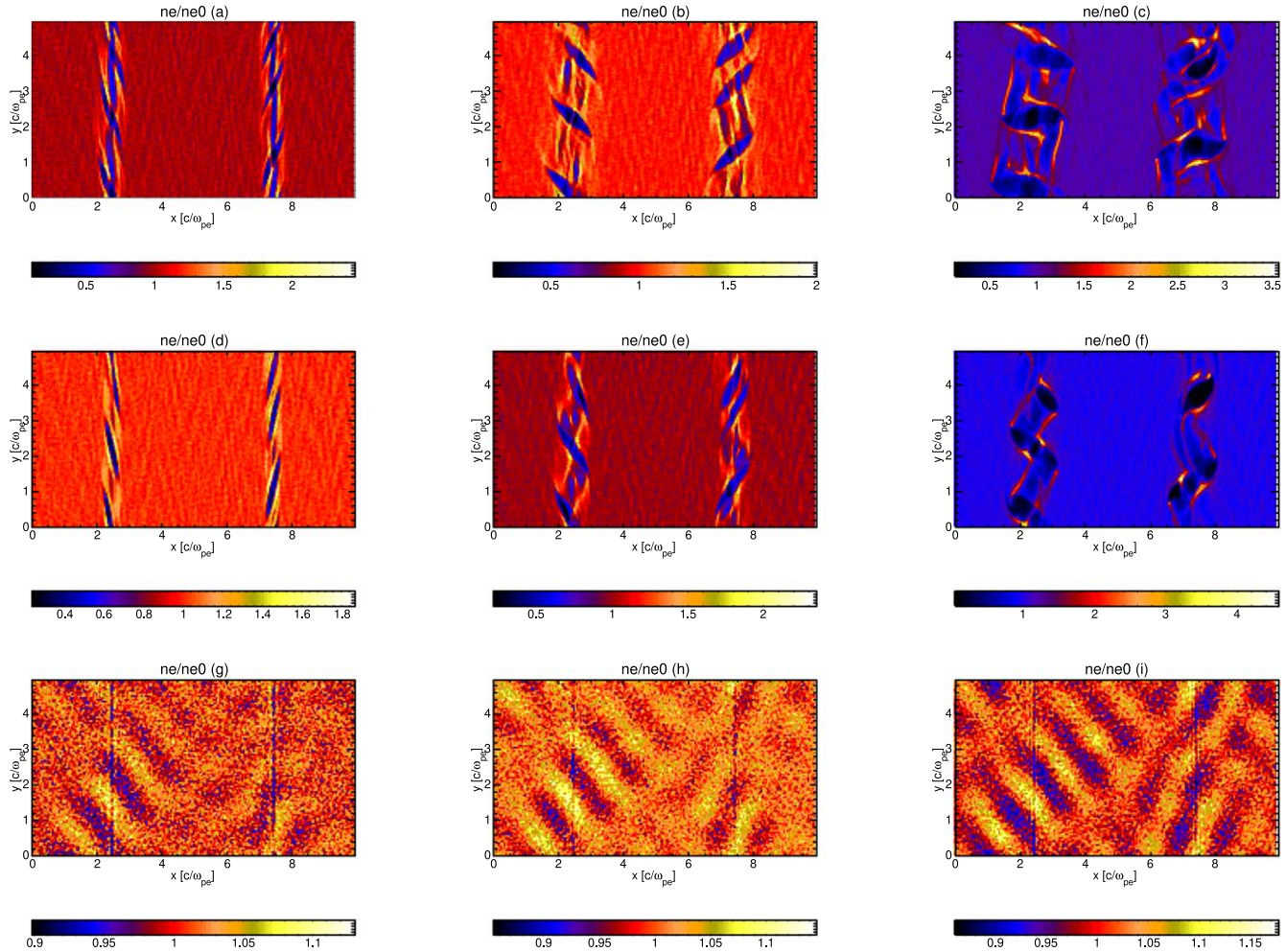

Figure 1. Snapshots of electron number density n_e. The row of panels (a), (b), and (c) shows n_e/n_0 for Run 0 at times $t = 20, 25, 30/\omega_{pe}$ respectively. The row of panels (d), (e), and (f) shows n_e/n_0 for Run 2 at times $t = 20, 25, 30/\omega_{pe}$ respectively. The row of panels (g), (h), and (i) shows n_e/n_0 for Run 6 at twice the times $t = 40, 50, 60/\omega_{pe}$ respectively. See Table 1 for details.

of panels (g), (h), and (i) shows n_e/n_0 for Run 6 at twice the times $t = 40, 50, 60/\omega_{pe}$ respectively. We gather from Figure 1 that in the case of zero external magnetic field (Run 0), the elongated, rotating vortices are progressively generated. We note significant similarities of panels corresponding Run 0 to a similar numerical run with the same number density across the shear interface from Alves et al. (2014), see their Figure 6. The vortices start as narrow elongated flow structures with under-dense cores $n_e/n_0 \simeq 0.5$ and strongly over-dense edges $n_e/n_0 \simeq 2$. Note the values on the color bar. As the time progresses from 20 to $30/\omega_{pe}$, the vortex core-edge contrasts deepen even further and the width of vortices grows. Such large values of under- and over-density indicate strongly nonlinear evolution of these ESKHI-generated vortices. As the external magnetic field is increased (Run 2) the values of under- and over-density in the vortices drop initially. In the case of $\bar{B}_0 = B_{y0}/B_{MHD} \gg 1$ (Run 6), vortices disappear altogether and only linear amplitude waves can be seen generated in the vicinity of the shear interfaces $x/L = 0.25$ and 0.75. As can be seen in Figure 1, panels (a)–(f), the simulation results are not affected by the periodic boundary conditions used, because across x-axis vortices never reach boundaries, but they simply leave and re-enter at the top and bottom boundaries across the y-axis.

We also note that in Figure 1, the electron number density has spatial variations in both the x- and y-directions. This is because the vortices formed by ESKHI are rotating in the xOy plane. The theoretical model presented in the Appendix only considers x-variation for the perturbations. Strictly speaking, our theoretical model should also have y-variation. However, we retain only x-variation for simplicity, because, as explained in the conclusions, we only use Equations (21)–(23), and what follows from them just to set the scale of two-fluid (non-relativistic) MHD stability threshold magnetic field, given by Equations (13) and (14), which we use in our PIC simulation as a relevant scale, B_{MHD}.

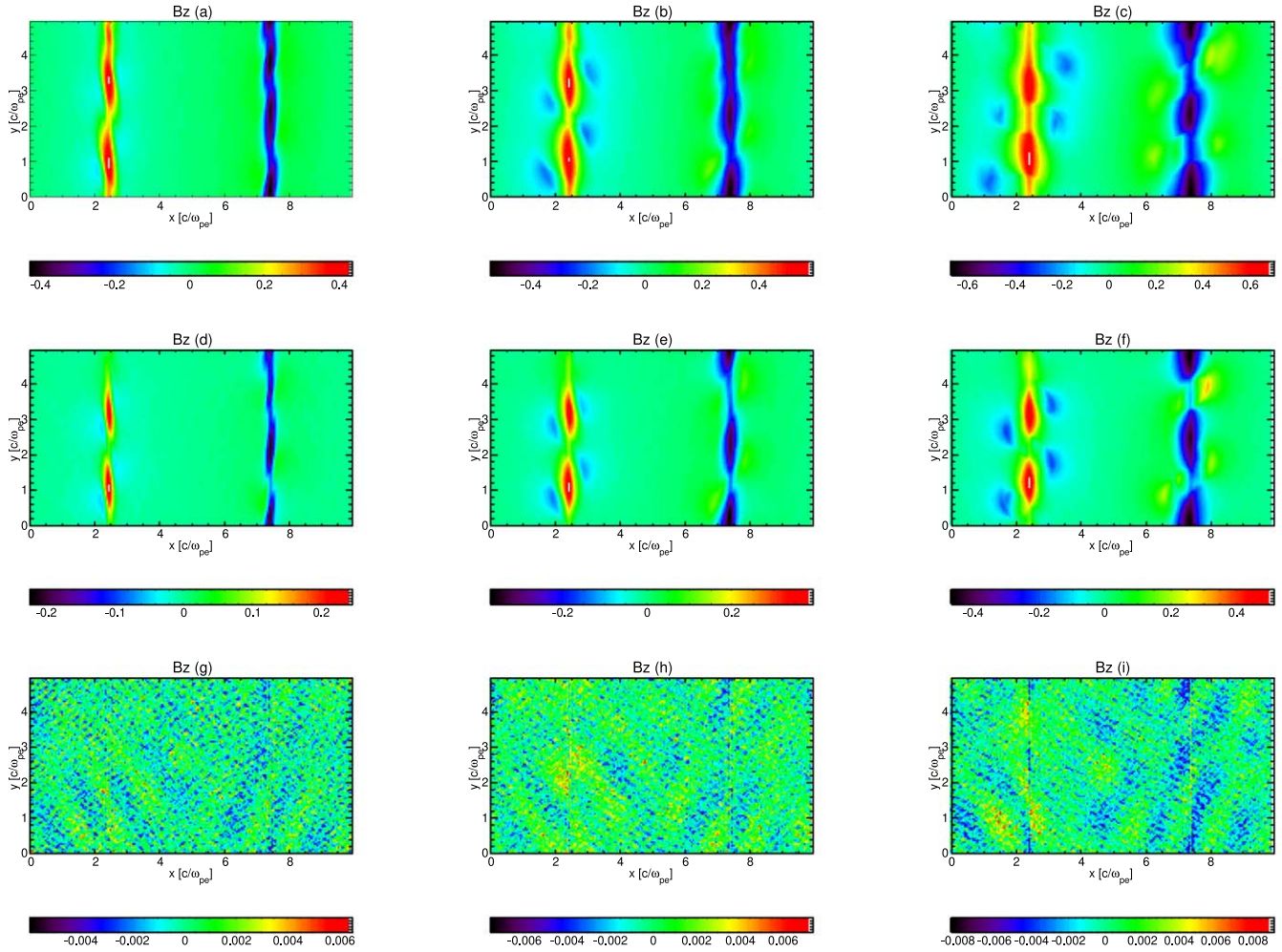

Figure 2. Snapshots of out-of-plane magnetic field B_z generated by the ESKHI. The numerical runs and the snapshot times are in direct correspondence to Figure 1.

Figure 2 has the purpose of quantifying how the out-of-plane magnetic field B_z is generated by the ESKHI. We see in Figure 2 that in the case of zero external magnetic field (Run 0) DC (although with a corrugated shape) magnetic field B_z is progressively generated in the vicinity of the shear interfaces $x/L = 0.25$ and 0.75. The values, judging from the color bar, range $\pm(0.4\text{–}0.6)B_{\rm MHD}$ and they grow as the time progresses from the left to right panels. Again, we mention that significant similarities can be seen in panels corresponding to Run 0, a similar numerical run with the same number density across the shear interface from Alves et al. (2014), see their Figure 7. For the further increased (increased from zero) external magnetic field, for Run 2, we see that the generated values of B_z are about a factor of two smaller compared to Run 0. Also, gaps in the generated DC field appear, as these structures further narrow down across the shear interfaces at $x/L = 0.25$ and 0.75. For Run 6, the values of B_z drop to 0.005 near the shear interfaces at $x/L = 0.25$ and 0.75.

In Figure 3 we show the time evolution of perturbation equipartition energy $(E_B - E_B(0))/E_p(0)$. It is crucial that we subtract $E_B(0)$ because we want to separate the pre-existing magnetic field energy contribution from the ESKHI-generated magnetic field energy. We calculate this quantity in the following way: at every time step, we load the data and calculate the following quantity

$$\begin{aligned}&\frac{E_B(t) - E_B(0)}{E_p(0)}\\ &= \iint \frac{b_x(x, y, t)^2 + [b_y(x, y, t) - B_{y0}]^2 + b_z(x, y, t)^2}{2\mu_0 E_p(0)} dxdy\\ &= \frac{1}{2\mu_0 E_p(0)} \sum_{i=1}^{n} [b_x(x_i, y_i, t)^2 + [b_y(x_i, y_i, t) - B_{y0}]^2\\ &\quad + b_z(x_i, y_i, t)^2] \Delta x \Delta y. \end{aligned} \tag{30}$$

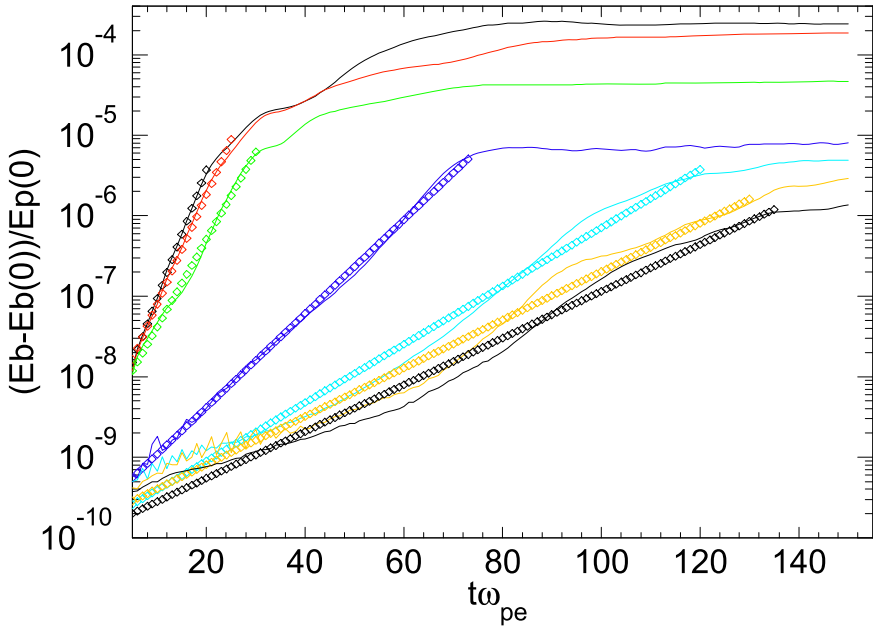

Figure 3. Black, red, green, blue, cyan, gold, and thick solid curves show $(E_B - E_B(0))/E_p(0)$ using numerical simulation data from Run0—Run 6 using Equation (30). The open diamonds with the same multi-colors are showing the fit using Equation (31).

Note that in Equation (30) the numerical integration is done by the midpoint rule (also known as the rectangle rule). In Figure 3 black, red, green, blue, cyan, gold, and thick solid curves show $(E_B - E_B(0))/E_p(0)$ using numerical simulation data from Run0—Run 6 applying Equation (30). We gather that ESKHI rapidly grows the magnetic perturbation equipartition energy on the timescales of 30 to $120/\omega_{\rm pe}$ depending on the strength of the background external magnetic field. This exponential growth phase is followed by a plateau which, as explained by Alves et al. (2014), is due to the magnetic field component B_z *generated* by ESKHI that blocks the flow of electrons across the shear interfaces at $x/L = 0.25$ and 0.75. We also see that as $\bar{B}_0 = B_{y0}/B_{\rm MHD}$ increases from 0 to 15, the growth rate of ESKHI decreases considerably. The open diamonds of the same color, as stated above, show our fit using the following method. We use Interactive Data Language (IDL)'s built-in function called `poly_fit` to calculate $r[0]_i$ and $r[1]_i$ that appear in Equation (31), where $i = 0,\ldots, 6$ for each of the Run0—Run 6. Effectively, this function fits a 1st order polynomial to the natural logarithm of $(E_B - E_B(0))/E_p(0)$ with $r[0]_i$ and $r[1]_i$ being the 0th and 1st order fit coefficients to the polynomial respectively. This fit then enables plotting with open diamonds, visualizing the data fit using Equation (31)

$$e^{r_i[0]} \times e^{r_i[1]\omega_{\rm pe}t}. \quad (31)$$

The values of $r_i[1]$ are quoted as the 3rd column of Table 1. Effectively these values are the growth rates of ESKHI $(\Gamma\omega_{\rm pe})_{\rm Diam} = $ `r_i[1]` shown with multi-color open diamonds in Figure 3. "Diam" is the abbreviation for diamonds from Figure 3.

Table 1
Table of Numerical Runs Considered

Run	$\bar{B}_0 = B_{y0}/B_{\rm MHD}$	$(\Gamma\omega_{\rm pe})_{\rm Diam} =$ `r_i[1]`	$(\Gamma\omega_{\rm pe})_{\rm Fit}$
0	0.0	0.3667	0.3663
1	0.5	0.3138	0.3061
2	1.0	0.2504	0.2629
3	5.0	0.1340	0.1234
4	7.5	0.0834	0.0927
5	10.0	0.0690	0.0742
6	15.0	0.0668	0.0531

Note. See text discussing Figure 3 for the explanation of the notation used.

In Figure 4 we would like to deduce the effect of external magnetic field on ESKHI in a functional dependence form. In other words, we would like to know what function can be fitted to $(\Gamma\omega_{\rm pe})_{\rm Diam}$. Various plausible functions were attempted. Only a small fraction of fit functions is displayed in panels (a)–(f) in Figure 4. We gather from Figure 4 that in panel (c) we have the best fit with the smallest errors. Thus we conclude that the best fit is hyperbolic, $\Gamma(B_0)\omega_{\rm pe} = \Gamma_0\omega_{\rm pe}/(A + B\bar{B}_0)$, where $\Gamma_0\omega_{\rm pe} = 1/\sqrt{8} = 0.35$ is the ESKHI growth rate without external magnetic field and $\bar{B}_0 = B_0/B_{\rm MHD}$ is the ratio of external and two-fluid MHD stability threshold magnetic field. The hyperbolic fit numerical values of the growth rate are quoted for reference as the 4th column in Table 1. Indeed, as can be deduced both from Figure 4(c) and the 3rd and 4th columns in Table 1, the fit graphically and numerically is rather good. The factor, which is the x-axis in

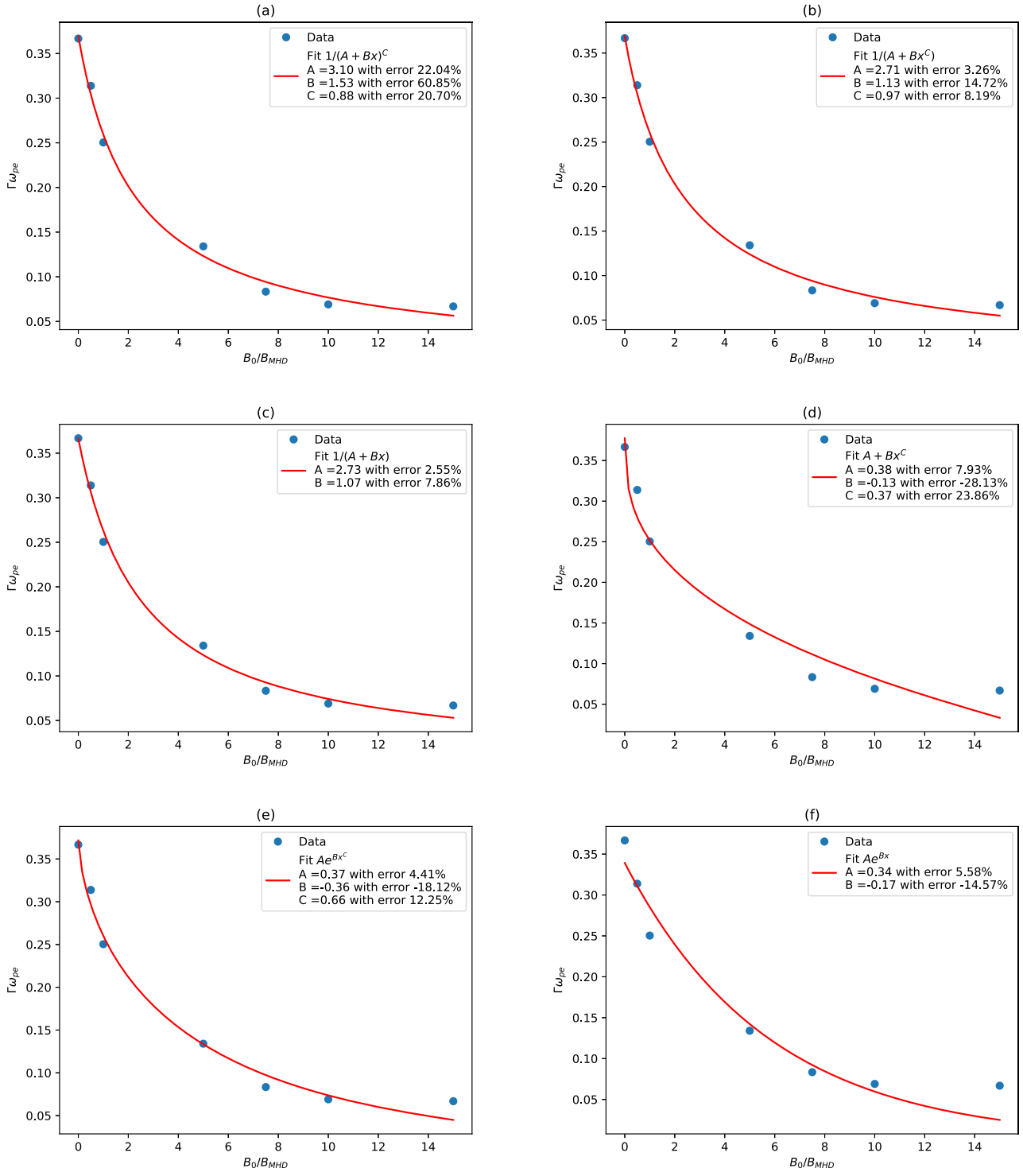

Figure 4. Various plausible functions fitted to $(\Gamma\omega_{\rm pe})_{\rm Diam}$ values, i.e., the best possible functional fit to the 3rd column of Table 1.

Figure 4, with $\bar{B}_0 = 0$, 0.5, 1.0, 5.0, 7.5, 10.0, 15.0 provides a variation for the external magnetic field. Paradoxically, for the growth rate predicted by Equation (26) which is supposed to be the best fit, the fit does not even converge due to large errors.

In Figure 5, we show the time evolution of particle perturbation kinetic energy $(E_p - E_p(0))/E_p(0)$ using numerical simulation data from Run0—Run 6 with the same multi-color curves as in Figure 3. We deduce two observations from

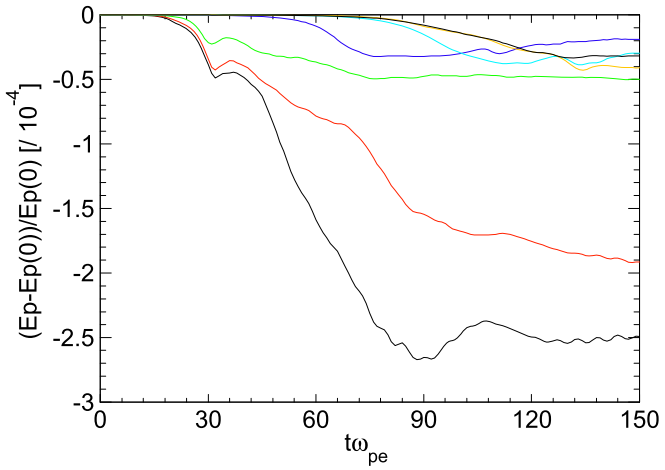

Figure 5. Time evolution of particle perturbation kinetic energy $(E_p - E_p(0))/E_p(0)$ using numerical simulation data from Run 0—Run 6 with the same multi-color curves as in Figure 3.

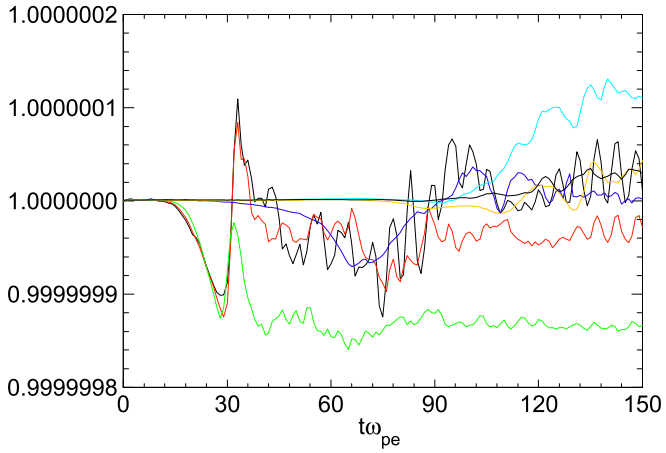

Figure 6. Similar to Figure 5 but now for the total energy.

Figure 5: (i) The magnetic field generated by ESKHI comes at the expense of a reduction in particle kinetic energy; (ii) The strongest reduction in the kinetic energy is seen for the case of Run 0, a zero background external magnetic field when the ESKHI growth rate is the largest. As the external magnetic field is increased, this arrests the flow of electrons across the shear interfaces and we see lesser and lesser reduction in the kinetic energy, as a result of this.

In Figure 6, we plot the total energy $(E_p + E_f)/(E_p(0) + E_f(0))$ in a similar manner to Figure 5. Note that E_f denotes the total electromagnetic (EM) field energy, automatically calculated by EPOCH as `data.TOTAL_FIELD_ENERGY`, which includes contribution from both magnetic and electric fields, while in Figure 3 we had to calculate perturbation equipartition energy $(E_B - E_B(0))/E_p(0)$ manually, using Equation (30). We gather from Figure 6 that the total energy conservation in all our EPOCH numerical runs is superb and the relative errors are contained within a small margin of ± 0.0000001 i.e., $\pm 0.00001\%$.

5. Conclusions

ESKHI can be of importance in many collisionless plasmas, e.g., when solar wind interacts with planetary magnetospheres, a magnetic field that is generated in AGN jets, or shocks and flows found in GRBs (Gruzinov 2008; Alves et al. 2012; Grismayer et al. 2013; Alves et al. 2014, 2015). The aim of this paper is to study the effect of an external, background magnetic field on ESKHI. Thus we use PIC, fully electromagnetic plasma simulation as the main tool for this purpose. This study finds that in the kinetic regime, the presence of an external magnetic field reduces the growth rate of the instability—a result similar to the well-known analog—MHD KHI. While in MHD there is a known threshold magnetic field for KHI stabilization as first shown by Michael (1955), for ESKHI this is yet to be determined by an appropriate analytical calculation that would extend the approach used in Alves et al. (2014, 2015) by adding the external, background magnetic field. Such calculation is rather complex if all three components of velocity v_x, v_y, v_z are considered. Note that in EPOCH, in all versions: 1.5, 2.5, 3D, all three components of velocity are always present. Instead, for the purposes of this paper, we only use the calculations based on Equations (21)–(23), and their outcomes to set the scale of a two-fluid MHD stability threshold magnetic field, derived in the Appendix and given by Equation (14). As it stands, without a fully kinetic analytical expression for the growth rate, we decided to use several numerical simulation runs to find an empirical dependence of ESKHI growth rate, $\Gamma(B_0)\omega_{pe}$, on the strength of the applied external magnetic field. Our results show that the best fit is hyperbolic, $\Gamma(B_0)\omega_{pe} = \Gamma_0\omega_{pe}/(A + B\bar{B}_0)$. We note an urgent need for an analytical theory to back up the said growth rate dependence on the external magnetic field. The first peculiar and important result that follows from our study is that in astrophysical objects where a strong magnetic field pre-exists, the generation of an additional magnetic field by the ESKHI is suppressed. The latter suggests that with this, nature provides a "safety valve"—natural protection not to "over-generate" magnetic field. The second peculiar result is that we show that a two-fluid (non-relativistic) MHD threshold magnetic field, calculated in Appendix, (Equation (13) or equally Equation (14)) is the same (up to a factor of $\sqrt{\gamma_0} \approx 1$) as the DC saturation magnetic field, predicted by the fully kinetic theory (Equation (9)) established by Grismayer et al. (2013), Alves et al. (2014).

This work was completed when the author became aware (G.P. Zank, 2024, private communication) of Che & Zank (2023). The calculation expressed in our Appendix and also our

Equation (27) appear to be similar to that of Che & Zank (2023). However, it is clear that neither Equation (41) of Che & Zank (2023) nor our Equations (24)–(26) agree with the best fit, $\Gamma(B_0)\omega_{\rm pe} = \Gamma_0\omega_{\rm pe}/(A + B\bar{B}_0)$, established by the present work. This disagreement means that a new analytical calculation for the same number density across the shear interface as in Alves et al. (2014) with added external magnetic field B_0 along the shear interface is needed. Further, the results from Table 1 can be used to check the validity of the said growth rate yet to be analytically determined. Such analytical theory to back up what is established here by PIC simulation growth rate dependence on the external magnetic field is urgently needed. We stress again that we only use the calculations based on Equations (21)–(23) and their outcomes to set the scale of two-fluid (non-relativistic) MHD stability threshold magnetic field, given by Equations (13) and (14), used in our PIC simulation as a relevant scale, $B_{\rm MHD}$.

Acknowledgments

The author would like to thank an anonymous referee whose comments improved this manuscript.

Data Availability

The data that support the findings of this study are available from the corresponding author upon reasonable request.

Appendix

Starting with the equations of two-fluid MHD with stationary ions (21)–(23), we consider two magnetized electron flows with properties ρ_{e1}, p_{e1}, U_{e1}, B_1 for $y<0$ and ρ_{e2}, p_{e2}, U_{e2}, B_2 for $y>0$ with the interface at $y=0$. We only consider the xOy plane. This calculation extends that of Michael (1955) two-fold: (i) we consider the situation where the bulk flow velocity is replaced by electron velocity, $\boldsymbol{v} \to \boldsymbol{v}_e$, and $\rho \to \rho_e$; and (ii) the densities across the interface are different. For $y<0$ we have the following linearized equations in the component form:

$$\frac{\partial b_x}{\partial t} + U_{e1}\frac{\partial b_x}{\partial x} = B_1\frac{\partial v_{ex}}{\partial x}, \tag{A1}$$

$$\frac{\partial b_y}{\partial t} + U_{e1}\frac{\partial b_y}{\partial x} = B_1\frac{\partial v_{ey}}{\partial x}, \tag{A2}$$

$$\frac{\partial v_{ex}}{\partial t} + U_{e1}\frac{\partial v_{ex}}{\partial x} = -\frac{1}{\rho_{0e1}}\frac{\partial p_{e1}}{\partial x}, \tag{A3}$$

$$\frac{\partial v_{ey}}{\partial t} + U_{e1}\frac{\partial v_{ey}}{\partial x} = -\frac{1}{\rho_{0e1}}\frac{\partial p_{e1}}{\partial y} + \frac{B_1}{\mu_0\rho_{0e1}}\left(\frac{\partial b_y}{\partial x} - \frac{\partial b_x}{\partial y}\right), \tag{A4}$$

$$\frac{\partial b_x}{\partial x} + \frac{\partial b_y}{\partial y} = 0, \qquad \frac{\partial v_{ex}}{\partial x} + \frac{\partial v_{ey}}{\partial y} = 0, \tag{A5}$$

where $v_{ex,ey}$ and $b_{x,y}$ are the perturbations of background values of U_{e1} and B_1. Next, we substitute in Equations (A1)–(A5) a Fourier ansatz of the form $f = \tilde{f}\, e^{i(kx+\omega t)}$ and omit the tilde signs:

$$i(\omega + kU_{e1})b_x = B_1 ikv_{ex}, \tag{A6}$$

$$i(\omega + kU_{e1})b_y = B_1 ikv_{ey}, \tag{A7}$$

$$i(\omega + kU_{e1})v_{ex} = -\frac{ik}{\rho_{0e1}}p_{e1}, \tag{A8}$$

$$i(\omega + kU_{e1})v_{ey} = -\frac{1}{\rho_{0e1}}\frac{\partial p_{e1}}{\partial y} + \frac{B_1}{\mu_0\rho_{0e1}}\left(ikb_y - \frac{\partial b_x}{\partial y}\right), \tag{A9}$$

$$ikb_x + \frac{\partial b_y}{\partial y} = 0, \tag{A10}$$

$$ikv_{ex} + \frac{\partial v_{ey}}{\partial y} = 0. \tag{A11}$$

Equations (A6)–(A11) can be combined into one master equation for v_{ey}:

$$\left(\frac{B_1^2k^2}{\mu_0\rho_{0e1}} - (\omega + kU_{e1})^2\right)\left(k^2v_{ey} - \frac{\partial^2 v_{ey}}{\partial y^2}\right) = 0. \tag{A12}$$

Following a similar approach to Michael (1955), from Equation (A12) we have a solution for $y<0$ (medium 1) $v_{ey1} = C_{11}e^{ky} + C_{12}e^{-ky}$. For a solution that approaches zero as $y \to -\infty$ we have $v_{ey1} = C_{11}e^{ky}$. Likewise, in the region with $y>0$ (medium 2), for a solution that approaches zero as $y \to \infty$ we have $v_{ey2} = C_{22}e^{-ky}$.

Let $\xi(x, t)$ be displacement of the interface satisfying a condition $\xi \ll 2\pi/k = \lambda$. As in Michael (1955), based on the definition $v_{ey1} = \partial\xi/\partial t + U_{e1}\partial\xi/\partial x$ and $v_{ey2} = \partial\xi/\partial t + U_{e2}\partial\xi/\partial x$, we demand continuity of $\partial\xi/\partial t$:

$$\frac{\partial \xi}{\partial t} = v_{ey1} - U_{e1}\frac{\partial \xi}{\partial x} = v_{ey2} - U_{e2}\frac{\partial \xi}{\partial x}, \tag{A13}$$

which at the interface $y=0$ yields

$$(\omega + kU_{e1})C_{11} = (\omega + kU_{e2})C_{22}. \tag{A14}$$

We also have to fulfill the condition for the pressure balance $p_e + B^2/(2\mu_0) = \text{const}$, substituting $p_e = p_{e0} + p_{e1}$ and $B = B_{1,2} + b_{1,2}$, at the interface, at a linear order. Omitting the quadratic terms, at the interface $y=0$ we obtain

$$p_{e1} + \frac{B_1 b_{x1}}{\mu_0} = p_{e2} + \frac{B_2 b_{x2}}{\mu_0}. \tag{A15}$$

Substituting the following quantities for medium 1

$$p_{e1} = \frac{-i(\omega + kU_{e1})\rho_{e1}C_{11}}{k}, \tag{A16}$$

$$b_{x1} = \frac{ikB_1C_{11}}{(\omega + kU_{e1})}, \tag{A17}$$

and similar expressions for medium 2

$$p_{e2} = \frac{i(\omega + kU_{e2})\rho_{e2}C_{22}}{k}, \tag{A18}$$

$$b_{x2} = -\frac{ikB_2C_{22}}{(\omega + kU_{e2})}, \tag{A19}$$

into Equation (A15) and after multiplying both sides by k, we obtain

$$C_{11}\left(-(\omega + kU_{e1})\rho_{e1} + \frac{B_1^2k^2}{\mu_0(\omega + kU_{e1})}\right) = C_{22}\left((\omega + kU_{e2})\rho_{e2} - \frac{B_2^2k^2}{\mu_0(\omega + kU_{e2})}\right). \tag{A20}$$

The next step is to make use of Equation (A14) to obtain

$$\frac{\left(-(\omega + kU_{e1})\rho_{e1} + \frac{B_1^2k^2}{\mu_0(\omega + kU_{e1})}\right)}{(\omega + kU_{e2})} = \frac{\left((\omega + kU_{e2})\rho_{e2} - \frac{B_2^2k^2}{\mu_0(\omega + kU_{e2})}\right)}{(\omega + kU_{e1})}. \tag{A21}$$

Further, simple algebra leads us to a quadratic equation

$$(\rho_{e1} + \rho_{e2})\omega^2 + 2k(U_{e1}\rho_{e1} + U_{e2}\rho_{e2})\omega + \left[k^2(U_{e1}^2\rho_{e1} + U_{e2}^2\rho_{e2}) + \frac{B_1^2k^2}{\mu_0} + \frac{B_2^2k^2}{\mu_0}\right] = 0. \tag{A22}$$

Equation (A22) is a quadratic equation with respect to ω, which has the solution given by Equation (24).

ORCID iDs

D. Tsiklauri https://orcid.org/0000-0001-9180-4773

References

Alves, E. P., Grismayer, T., Fonseca, R. A., & Silva, L. O. 2014, NJPh, 16, 035007
Alves, E. P., Grismayer, T., Fonseca, R. A., & Silva, L. O. 2015, PhRvE, 92, 021101
Alves, E. P., Grismayer, T., Martins, S. F., et al. 2012, ApJ, 746, L14
Arber, T. D., Bennett, K., Brady, C. S., et al. 2015, PPCF, 57, 113001
Blandford, R. D., & Pringle, J. E. 1976, MNRAS, 176, 443
Chandrasekhar, S. 1961, Hydrodynamic and Hydromagnetic Stability (New York: Dover)
Che, H., & Zank, G. P. 2023, PhPl, 30, 062110
Cho, J., & Lazarian, A. 2009, ApJ, 701, 236
Delamere, P. A., Barnes, N. P., Ma, X., & Johnson, J. R. 2021, FrASS, 8, 801824
Delamere, P. A., Wilson, R. J., & Masters, A. 2011, JGRA, 116, A10222
Foullon, C., Verwichte, E., Nakariakov, V. M., Nykyri, K., & Farrugia, C. J. 2011, ApJL, 729, L8
Gordeev, A., Kingsep, A., & Rudakov, L. 1994, PhR, 243, 215
Grismayer, T., Alves, E. P., Fonseca, R. A., & Silva, L. O. 2013, PhRvL, 111, 015005
Gruzinov, A. 2008, arXiv:0803.1182
Helmholtz, H. 1868, Ber.Akad.Wiss.Berlin, 23, 215
Johnson, J. R., Wing, S., & Delamere, P. A. 2014, SSRv, 184, 1
Kelvin, L. 1871, PMag, 42, 362
Liang, E., Boettcher, M., & Smith, I. 2013a, ApJL, 766, L19
Liang, E., Fu, W., Boettcher, M., Smith, I., & Roustazadeh, P. 2013b, ApJL, 779, L27
Lyutikov, M. 2013, PhRvE, 88, 053103
Mahdavi-Gharavi, M., Mehdian, H., & Hajisharifi, K. 2020, AdSpR, 65, 1607
Michael, D. H. 1955, PCPS, 51, 528
Miller, E. D., & Rogers, B. N. 2016, JPlPh, 82, 905820205
Miura, A., & Pritchett, P. L. 1982, JGR, 87, 7431
Nishikawa, K.-I., Hardee, P., Zhang, B., et al. 2013, AnGeo, 31, 1535
Nishikawa, K.-I., Hardee, P. E., Dutan, I., et al. 2014, ApJ, 793, 60
Piran, T. 2005, RvMP, 76, 1143
Tsiklauri, D. 2023, MNRAS, 527, 10822
Yao, P., Cai, H., Yan, X., et al. 2020, MRExt, 5, 054403
Zhao, J. S., Lu, J. Y., & Wu, D. J. 2010, ApJ, 714, 138